Progress In Electromagnetics Research, Vol. 166, 95–105, 2019

Phaseless Microwave Imaging of Dielectric Cylinders: An Artificial Neural Networks-Based Approach

Jesús E. Fajardo[1], Julián Galván[2], Fernando Vericat[1], C. Manuel Carlevaro[1, 3], and Ramiro M. Irastorza[*, 1, 4]

Abstract—An inverse method for parameters estimation of dielectric cylinders (dielectric properties, location, and radius) from amplitude-only microwave information is presented. To this end two different Artificial Neural Networks (ANN) topologies were compared; a Multilayer Perceptron (MLP) and a Convolutional Neural Network (CNN). Several two-dimensional (2D) simulations, with different sizes and locations of homogeneous dielectric cylinders employing the Finite Differences Time Domain (FDTD) method, were performed to generate training, validation, and test sets for both ANN models. The prediction errors were lower for the CNN in high Signal-to-Noise Ratio (SNR) scenarios, although the MLP was more robust in low SNR situations. The CNN model performance was also tested for 2D simulations of dielectrically homogeneous and heterogeneous cylinders placed in acrylic holders showing potential experimental applications. Moreover, the CNN was also tested for a three-dimensional model simulated as realistic as possible, showing good results in predicting all parameters directly from the S-parameters.

1. INTRODUCTION

Inverse problem in microwave imaging from phaseless data (amplitude-only) is a challenging problem [1]. It gained attention because of simple measurement apparatuses requirements and its consequent reduction of costs. To solve this problem, two main approaches were proposed: using phase retrieval methods [2] and reconstructing the scatterers directly from measurements [3]. In the former, the phase was estimated from the amplitude-only data, and then amplitude and phase were used with the traditional reconstruction algorithms. Latter, several approaches were developed using deterministic [4, 5] and stochastic methods [6, 7]. As a stochastic method, ANN have advantageous capabilities to account for nonlinear effects which are present in inverse scattering problems [8]. A variety of inverse scattering ANN-based approaches were developed, including hybrid methods combining ANN and iterative methods [9]. Particularly for phaseless scenarios, one of the first works in this direction was proposed in the earliest 2000's by Bermani et al. [6]. The authors employed an MLP to solve (not simultaneously) two problems: reconstructing the dielectric properties of a cylinder, with known radius and position, and detecting the position of a buried cylinder, with known dielectric properties and radius.

In the field of Deep Learning, the improvements which provide CNN respect to MLP networks for recognizing patterns in images and complex data are notorious [10]. Recently, some works presented different CNN-based approaches for solving the inverse scattering problem, showing the potential of the

Received 6 August 2019, Accepted 2 December 2019, Scheduled 17 December 2019
* Corresponding author: Ramiro M. Irastorza (rirastorza@iflysib.unlp.edu.ar).
[1] Instituto de Física de Líquidos y Sistemas Biológicos CONICET - CCT La Plata, Argentina. [2] Instituto Argentino de Radioastronomía CONICET - CCT La Plata, Argentina. [3] Grupo de Materiales Granulares, Departamento de Ingeniería Mecánica, FRLP, Universidad Tecnológica Nacional, La Plata, Argentina. [4] Instituto de Ingeniería y Agronomía, UNAJ, Florencio Varela, Argentina.

model [8, 11, 12]. The CNNs of these works are based on the U-Net [13] and use both, amplitude and phase information. Surprisingly, to our knowledge, the CNN for solving the microwave Electromagnetic (EM) inverse problem with amplitude-only information has not been employed yet. In this work, we implemented such a topology and compared the results with an MLP. We computationally addressed the inverse scattering problem of estimating simultaneously dielectric and geometric parameters of an infinite cylinder. The homogeneous cylinder was illuminated by a circular array of monopole antennas (similar to the array presented by Meaney et al. [15]), and the electric field magnitude was computed by FDTD in a 2D simplified model. Such simulations were used to train the ANN. Using the trained ANN, particularly the CNN, heterogeneous cylinders were evaluated as well, and the predicted effective parameters are commented. In order to show the validity of the method, a full three-dimension simulation (using Finite Element Method (FEM)) was also provided, in which the whole setup was modeled as realistic as possible.

2. MATERIALS AND METHODS

2.1. Direct EM Scattering Problem Solution

The EM direct problem was solved using FDTD, implemented with the free available software MEEP [16]. The transmitter monopole antenna was considered as a line of current (a point source in 2D) emitting a TM-polarized electric field $E_z \propto e^{j\omega t}$, with "$z$" being the axis parallel to that of the antennas, $\omega = 2\pi f$, and f is the frequency of 1.1 GHz. The receiver antenna was not modeled, and the value of the electric field at the nearest point in the grid was collected instead. The geometry is a simplification of the one presented by Meaney et al. [15]. It consists of a circular array of 16 monopole antennas equally angularly spaced and disposed in a circle with a diameter of 15.2 cm. The object under study (e.g.: homogeneous cylinder) was placed within the investigation domain, which was a concentric circle with a diameter of 14.0 cm. The coupling bath was a glycerin-water mixture in 80 : 20 proportion with dielectric properties $\varepsilon_r = 28.6$ and $\sigma = 1.26\,\mathrm{Sm}^{-1}$ at 1.1 GHz. The size of the simulation box was 25 cm × 25 cm (with the array in the center); the spatial grid resolution of the simulation box was 1.0 mm; and the Courant factor was 0.5. The boundary conditions were Perfectly Matched Layers (PML), i.e., total absorption in the box edges.

In order to validate the FDTD models, the simulations were compared to analytical known results (not shown here) [17, 18]. A total of 10000 simulations of the direct EM problem were performed with different scatterer cylinders. The location, radius, and dielectric properties of the cylinders were randomly varied (uniform distributions) within the intervals described in Table 1. From these simulations the total field magnitude ($|E_t|$) was obtained. A simulation for the incident field magnitude ($|E_{inc}|$) was also computed (without the scatterer cylinder) for normalization purposes. The simulation of each particular cylinder implies that 16 (number of transmitters) × 16 (number of receivers excluding the transmitter) = 256 values were saved.

Table 1. Simulated range of the dielectric properties (at 1.1 GHz) and radius of the cylinder.

Radius (mm)	ε_r	σ (Sm^{-1})
[2.0, 30.0]	[10.0, 80.0]	[0.40, 1.60]

A whole setup simulation was also computed in 3D for validation purposes. Simulations were performed using *ad hoc* software applying the FEM approach (similar to the work of Attardo et al. [19]). The model is composed of: two monopole antennas (transmitter and receiver, which are modeled by a coaxial cable with the inner connector extended $\lambda/4$), the cylinder (with fixed position in the center of the array), and the acrylic tank container. The simulation box was a cube of 30 cm of side. The model mesh was heterogeneous, with a finer mesh size at the antennas interfaces. A total of around 200000 linear and triangular elements were used. The size of the finer mesh (around 0.2 mm) was estimated by a sensitivity analysis. A total of eight (one transmitter and eight receivers) 3D simulations were computed. The 256 data needed were obtained by the symmetry of the model (the cylinder is in the center).

2.2. Inverse Problem Using ANN

The inverse problem in microwave tomography is defined as reconstructing the object under study (the map of its dielectric properties which we called *the outputs*) sampling the data (*the inputs*) in the observation points (the circular array of 16 antennas). The inputs (x_i with $i = 1, \ldots, 256$) of the network corresponds to the ratio $|E_t|/|E_{inc}|$ normalized to the $[0, 1]$ interval ($16\times16 = 256$ values). The outputs (y_i with $i = 1, \ldots, 5$) of the model are: the coordinates of the cylinder center (X_{cen}, Y_{cen}), its radius, and the dielectric properties at 1.1 GHz (ε_r, σ). In this work, a simplified version of this problem is addressed by using ANN. It is basically a problem of minimization of the difference between the output of the model and the actual output.

The two kinds of networks commented below were implemented using the Application Programming Interface Keras [20] with Tensorflow [21] as backend package.

2.2.1. MLP Overview and Topology

An MLP ANN is an interconnected network of artificial neuron-like units, disposed in layers, where all the units of each layer are connected with all the units of the previous and next layer, but there are no connections between the units in the same layer. In this kind of ANN, the output of each layer is given by:

$$\mathbf{x}' = \mathbf{f}(\mathbf{W}\mathbf{x} + \mathbf{b}) \tag{1}$$

where $\mathbf{f}$ is the activation function of the layer; $\mathbf{W}$ is a matrix of adjustable parameters; $\mathbf{x}$ and $\mathbf{b}$ are, respectively, the input vector of the layer and a vector containing the bias term of each neuron of that layer. In general, in a network composed by N layers, the whole operation is a nested composition of these operations, given by:

$$\tilde{\mathbf{y}} = \mathbf{f_N}(\mathbf{W_N}\mathbf{f_{N-1}}(\cdots(\mathbf{W_2}\mathbf{f_1}(\mathbf{W_1}\mathbf{x} + \mathbf{b_1}) + \mathbf{b_2})\cdots + \mathbf{b_{N-1}}) + \mathbf{b_N}). \tag{2}$$

The input vector $\mathbf{x}$ is propagated through the network, and an output vector $\tilde{\mathbf{y}}$ of parameters is estimated. Then the result is compared to the actual $\mathbf{y}$ vector, and a loss is computed. Typically, one of the loss metrics used in such a regression is the Mean Absolute Percentage Error (MAPE), if the number of parameters is n (size of the vector $\mathbf{y}$) then:

$$\text{MAPE} = \frac{1}{n}\sum_{i=1}^{n}|\delta_i| \tag{3}$$

where

$$\delta_i = \frac{\tilde{y}_i - y_i}{y_i} \tag{4}$$

$\tilde{y}_i$ and y_i are the output of the model and the actual value of this i-th parameter (components of the vectors $\tilde{\mathbf{y}}$ and $\mathbf{y}$), respectively. In this work, we also computed the Mean Absolute Error (MAE) to avoid divergence in parameters that takes zero (or close to zero) values, which is directly computed as:

$$\text{MAE} = \frac{1}{n}\sum_{i=1}^{n}|\tilde{y}_i - y_i|\,. \tag{5}$$

After evaluating the loss, the gradients are retropropagated through the network from $\mathbf{y}$ to $\mathbf{x}$, and the weights are updated in all the neuron-like units composing the network in a direction opposite to that of the gradients $\nabla_\theta J(\theta)$, where $J(\theta)$ is the objective or loss function parameterized to the model parameters θ. Several approaches are used for doing this task [22]. Once the validation loss is low enough, and the network is capable of generalizing the prediction for new input vectors (not used during the training period), the matrices with the weights are saved, and its performance is evaluated in the test set.

The implemented topology is described in Table 2. A total of 6000 simulations were used for training, 2000 simulations were used for the the validation set (in order to prevent the model from overfitting), and 2000 simulations were reserved for test purposes. The input of the network corresponds to the ratio $|E_t|/|E_{inc}|$ normalized to the $[0, 1]$ interval. The output vector of the model is composed by 5 parameters: the coordinates of the cylinder center (X_{cen}, Y_{cen}), its radius, and dielectric properties

Table 2. Topology of the implemented MLP.

Input Layer	Hidden Layers	Output Layer
256 units	3×100 units	5 units
	Activation: ReLU	Activation: Linear

(ε_r, σ). As activation functions, Rectifier linear units (ReLU [23]) functions were used in all the neurons-like units, except in the output layer, where a general linear function was used. During the network training, a variation of the standard Gradient Descent (GD) method with adaptative momentum (presented by Kingma and Ba [24]) was used, which, for this particular study, outperformed that summarized in [22]. The selected loss function was MAPE (Eq. (3)), and 1000 epochs were required for convergence redwhile training the network with a batch size of 50.

2.2.2. CNN Overview and Topology

CNN can also be considered a nested composition of functions, from a d-dimensional input space $\mathbf{X} \in \mathbb{R}^d$ to $\mathbf{y} \in \mathbb{R}^n$, which is the output space of the inferred variables. The difference with respect to the MLP lies in the fashion that the internal operations are made, which allows the CNN to extract local features at different complexity levels. Particularly, the operation described by Eq. (1) changes into convolutional ones, which are the building blocks of CNNs and are defined on a translation invariance basis and have shared weights across different spatial locations. Both the input and output of convolutional layers are 2D matrices called feature maps, where the output feature map is obtained by convolving the kernels on the input feature map as:

$$\tilde{\mathbf{y}} = \mathbf{f}_{\mathrm{s}}(\mathbf{X}; \mathbf{W}, \mathbf{b}) = \mathbf{W} *_{\mathrm{s}} \mathbf{X} + \mathbf{b} \tag{6}$$

Here $\mathbf{X}$ is the input feature map; $\mathbf{W}$ and $\mathbf{b}$ denote kernel and bias, respectively; $*_{\mathrm{s}}$ represents convolution operation with stride s. As a result, the resolution of the output feature map $\mathbf{f}_{\mathrm{s}}(\mathbf{X}; \mathbf{W}, \mathbf{b})$ is downsampled by a factor of s. The output feature map of the last convolutional layer can then be fed into a stack of fully connected layers (MLP), which discard the spatial coordinates of the input and generates a global estimation for the input image-like matrix [10].

A detailed architecture of the implemented CNN is shown in Table 3. The sizes of the sets, number of epochs, the batch size, and GD method were the same as those used by the MLP. The input dimension also had the same input information used for the MLP, but reshaped to 16×16 image-like matrices (Fig. 1).

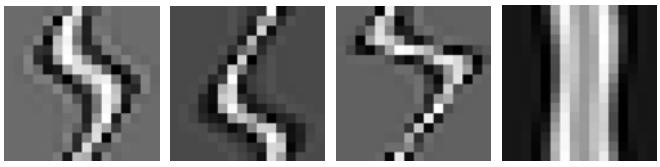

Figure 1. Input examples: black pixels corresponding to lower values and the white ones to higher values of the $|E_{\mathrm{t}}|/|E_{\mathrm{inc}}|$ ratio.

3. RESULTS AND DISCUSSION

3.1. MLP and CNN Comparison

We proposed an ANN similar to the one presented by Bermani et al. [6], but in our work the estimations are obtained simultaneously (dielectric and geometric properties). Comparison of the estimation quality for each parameter using both, the MLP and CNN models, are shown in Fig. 2. The histograms show the percent error of the dielectric parameters and the error in the geometric parameters. A good behaviour is observed for both MLP Networks and CNNs. Distributions of errors are zero centered and symmetric

Table 3. Topology of the implemented CNN.

Layer	Activation	Kernel	Filters	Input	Output
2D Conv.	ReLU	3×3 Stride: 1	32	(16, 16, 1)	(14, 14, 32)
2D Conv.	ReLU	3×3 Stride: 1	64	(14, 14, 32)	(12, 12, 64)
Pool	ReLU	2×2	64	(12, 12, 64)	(6, 6, 64)
Dense	ReLU	-	-	2304	100
Dense	ReLU	-	-	100	100
Dense	Linear	-	-	100	5

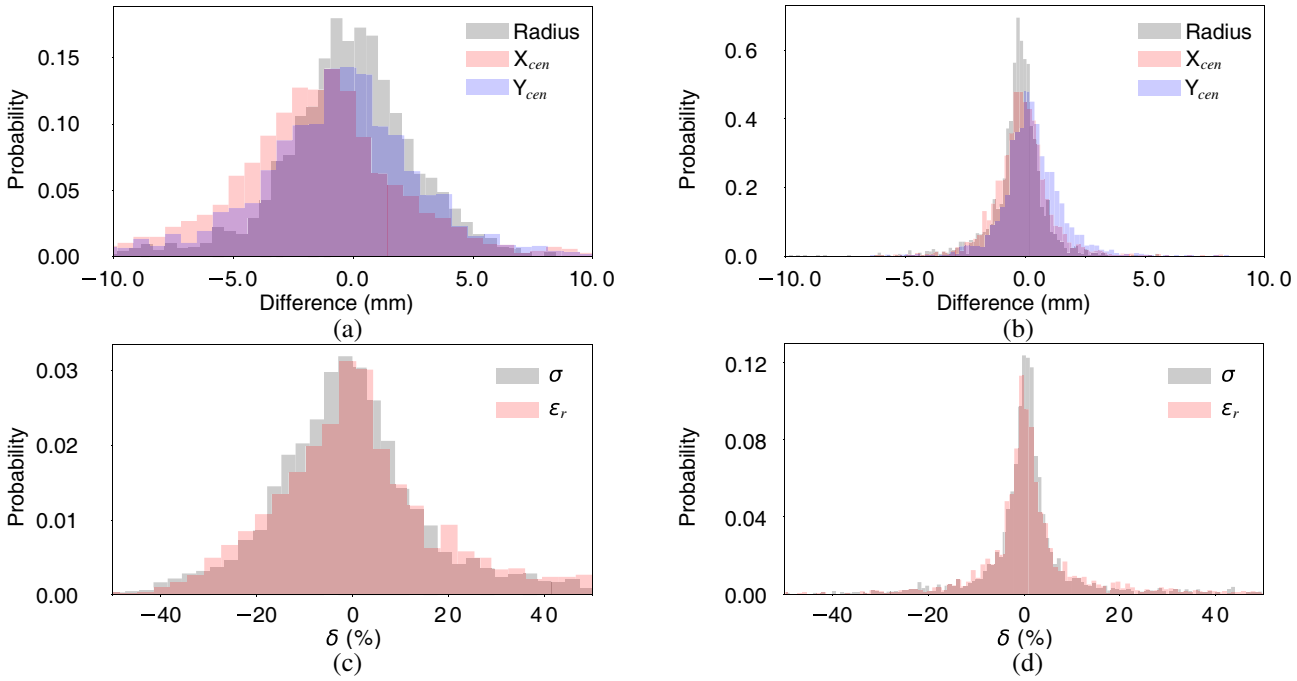

Figure 2. Histograms of geometric (a) and dielectric (c) estimation errors using the MLP model. Histograms of geometric (b) and dielectric (d) estimation errors using the CNN model.

bell-shaped. CNNs show considerably narrower distributions of the errors than MLP for both dielectric and geometric parameters.

In Fig. 3, the robustness of the models is tested for each parameter with different SNRs. This evaluation was performed by corrupting the test set data with Gaussian noise. In general, MLP networks were more robust than CNNs since with SNRs lower than 50 dB, lower errors were obtained. Particularly, the geometric properties estimation seems to have similar behaviours (see Figs. 3(a) and (b)). The worst performance was observed for the conductivity estimated by the CNNs for noise levels lower than 50 dB, and in this case relative errors of 100% were obtained. However, for SNR greater than 60 dB the CNNs always give better estimates of all the parameters.

Some reconstruction examples (with noise free data) for the cylinder dielectric properties, radius, and location using the CNN model described in Table 3 are shown in Fig. 4.

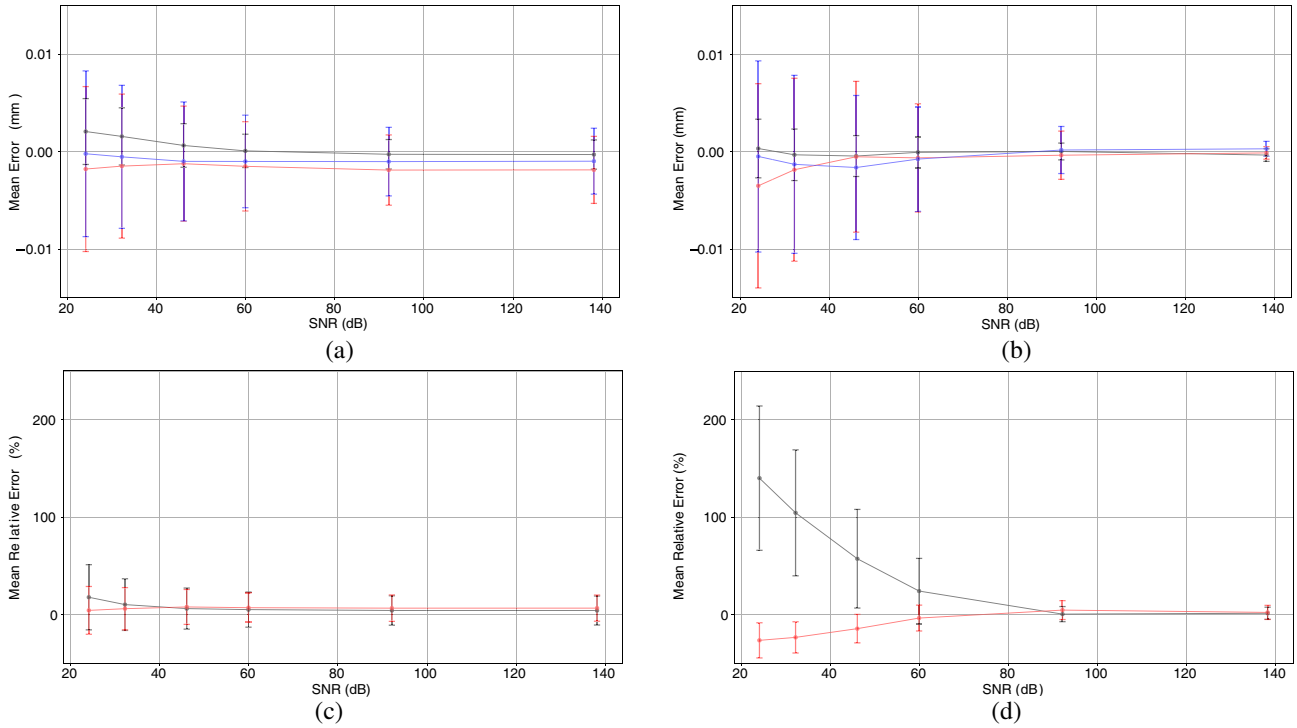

Figure 3. (a) X_{cen}, Y_{cen} and radius (red, blue and black lines, respectively) errors behaviour in presence of noise for the MLP model. (c) ε_r and σ (red and black lines, respectively) errors behaviour in presence of noise for the MLP model. (b) X_{cen}, Y_{cen} and radius (red, blue and black lines, respectively) errors behaviour in presence of noise for the CNN model. (d) ε_r and σ (red and black lines, respectively) errors behaviour in presence of noise for the CNN model. In all cases error bars represent the standard deviation.

3.2. Prediction of CNN: Homogeneous and Heterogeneous Samples

In this section, we study the behaviour of the previously obtained CNN for the prediction of a hypothetical experimental situation (with SNR greater than 60 dB): the cylinder to be measured should not be in contact with the coupling media. In order to fulfill this condition, the cylinder should be put into a sample holder. Two cases were evaluated: homogeneous cylinders and cylinders with cylindrical inclusions (heterogeneous) both into sample holders. We remark that the CNNs were trained with homogeneous cylinders (without holder), and consequently, the predictions for the dielectric parameters are effective (or equivalent) values.

3.2.1. Homogeneous Cylinder in Sample Container

We considered two sizes of acrylic sample holders with radii 9 mm and 18 mm, respectively. The thickness was $e = 0.5$ mm (see inset image in Fig. 5(a)), and the dielectric properties were $\varepsilon_r = 2.0$ and $\sigma \approx 0.0$ for both. Fifty simulations for each container were conducted varying the dielectric properties (within the range presented in Table 1) and the position (within the investigation domain) uniformly. The errors in the estimated geometric properties (MAE, see Eq. (5)) are shown in Table 4. Fig. 5 shows the results for the effective dielectric properties predictions. For the relative permittivity, the estimations fall on the straight line, then the acrylic container seems to not affect its measurement (Fig. 5(a)). Conductivity estimates are always lower than the actual values, and as expected, this effect worsens for the smaller container. However, it is a systematic error that can be corrected experimentally.

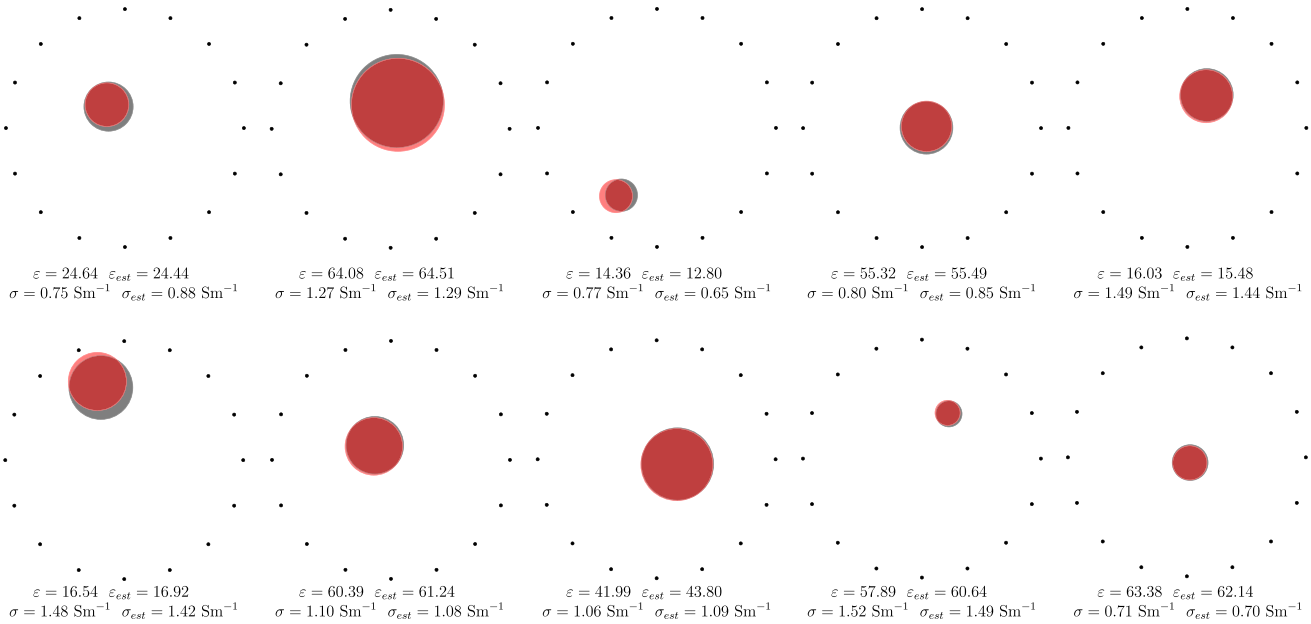

Figure 4. Reconstruction examples. The position of the antennas is shown with black dots. The gray circle represents the true cylinder cross-section, the red circle represents the CNN reconstruction. The values of ε_r and σ are also shown for the actual values and the estimated ones (subindex "est").

Table 4. Mean (standard deviation) of MAE for the estimated (using CNN) geometric parameters of the homogeneous and heterogeneous cylinders within an acrylic holder (all values expressed in mm).

Cylinder	radius	X_{cen}	Y_{cen}
Homogeneous (radius 0.9 cm)	0.21 (1.01)	0.25 (0.96)	0.15 (0.90)
Homogeneous (radius 1.8 cm)	0.36 (0.98)	0.15 (1.06)	0.64 (1.28)
Heterogeneous (case (a))	1.49 (7.15)	0.21 (1.56)	0.58 (1.43)
Heterogeneous (case (b))	3.39 (6.16)	0.42 (1.28)	0.39 (1.58)
Homogeneous 3D (radius 1.7 cm)*	1.28	0.59	0.03

* Only one simulation was computed.

3.2.2. Heterogeneous Cylinder in Sample Container

We also tested cylinders with cylindrical inclusions (constant radius, relative permittivity, and conductivity, $r_{\text{i}} = 2\,\text{mm}$, $\varepsilon_{r\text{i}} = 20$, and $\sigma_{\text{i}} = 0.7\,\text{Sm}^{-1}$, respectively) within an acrylic container (equal to the one of the previous section). The number of inclusions was varied to obtain different fractions of occupation, and overlap of inclusions was allowed. A sample with fraction of inclusion $\phi_{\text{i}} \approx 0.3$ is shown in the inset of Fig. 6(a). Two sets of dielectric properties of the background were evaluated: case (a) $\varepsilon_{r\text{b}} = 70$ and $\sigma_{\text{b}} = 1.4\,\text{Sm}^{-1}$; and case (b) $\varepsilon_{r\text{b}} = 30$ and $\sigma_{\text{b}} = 1.0\,\text{Sm}^{-1}$. It is important to remark that the radius of the sample and its position were also varied (within the range of Table 1 and the investigation domain, respectively).

There are several effective models (homogenisation of mixtures) to study dielectric samples with inclusions [25]. Two broadly used models in such problems are the Wiener bounds. Particularly, when the electric field is parallel to the direction of the fibers (inclusions of cylindrical shape), the Wiener bound takes the form:

$$\varepsilon^*_{\text{eff}} = \varepsilon^*_{\text{i}}\,\phi_{\text{i}} + \varepsilon^*_{\text{b}}\,(1 - \phi_{\text{i}}) \tag{7}$$

where $\varepsilon^*_j = \varepsilon_{r_j} - \sigma_j/(j\omega\epsilon_0)$ for each component (background and the inclusions, $j = \text{b}$ and $j = \text{i}$,

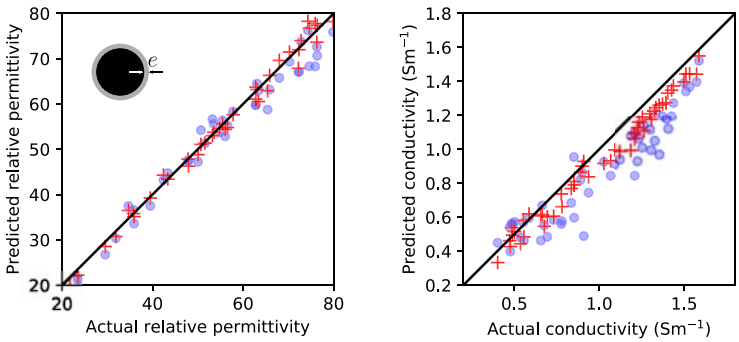

Figure 5. (a) Effective relative permittivity and (b) conductivity obtained by CNNs. The circles and crosses indicate the 9 mm and 18 mm radii, respectively. The inset shows the sample in the holder with thickness $e = 0.5$ mm.

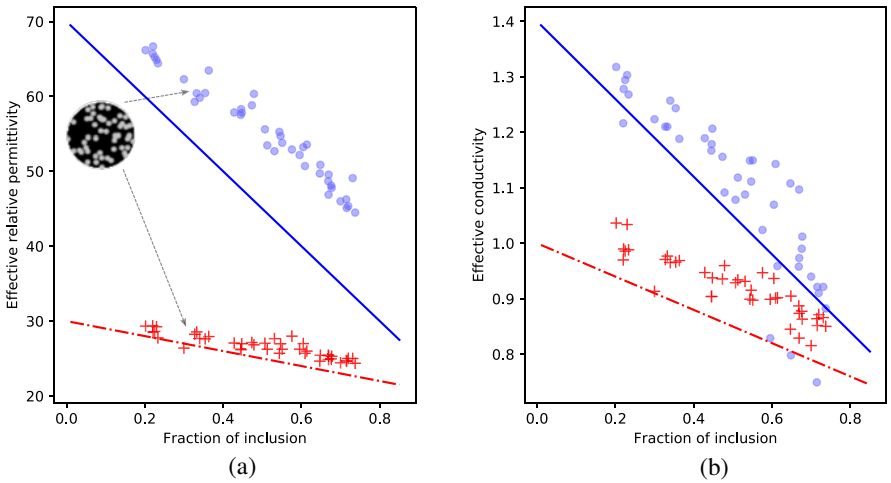

Figure 6. Heterogeneous cylinders with variable fraction of inclusion (ϕ_i) in holder. (a) Relative permittivity. (b) Conductivity. The red crosses and blue circles correspond to case (a) $\varepsilon_{rb} = 70$ and $\sigma_b = 1.4$ Sm^{-1}; and case (b) $\varepsilon_{rb} = 30$ and $\sigma_b = 1.0$ Sm^{-1}, respectively. The solid lines represent the Wiener models.

respectively). The effective relative permittivity and conductivity using this bound are also shown in Fig. 6. It can be seen that both dielectric properties show linear trends but differ from the Wiener bound. It is necessary to remark that the Wiener bound is not strictly the analytic behaviour that these samples would follow, because such a bound was developed for equally spaced layers, parallel to the electric field. For these heterogeneous samples, there is also a systematic error that can be corrected experimentally, and the fraction of occupation could be estimated (if the dielectric properties of inclusions and background are known). Table 4 shows the MAE for the estimated geometric parameters.

3.3. Comparison with a 3D Simulation

The training for both neural networks (MLP and CNN) is a computationally intensive and time consuming process. Consequently, in order to evaluate several scenarios and conditions it is better to simulate simple models. In this section, models in 3D were computed in order to simulate the whole experimental setup with detailed version of the antennas. These conditions determine a computationally heavy model unfeasible for training purposes. Therefore, in the inverse problem we used the ANNs trained with 2D homogeneous cylinders. In such a way, it is a validation of the inverse algorithms, which were trained with computationally lighter models.

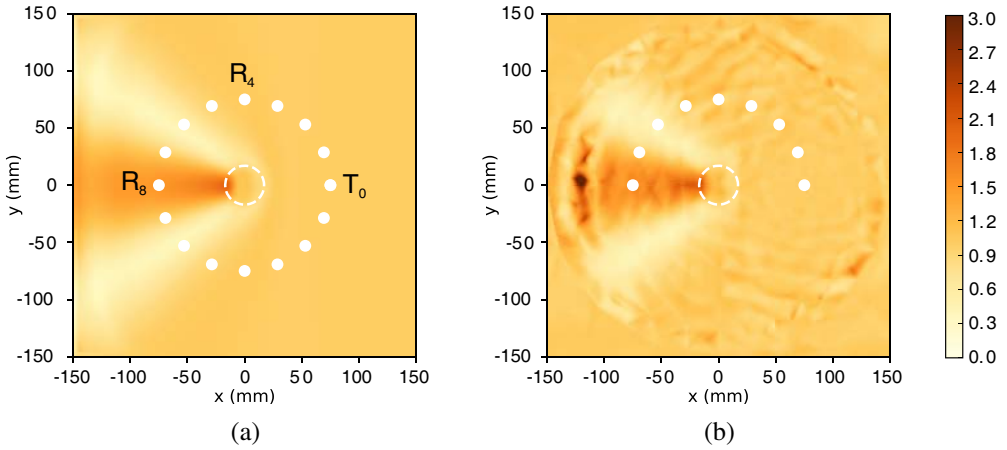

Figure 7. Input of the ANN ($|E_t|/|E_{inc}|$) obtained by simulation of a homogeneous cylinder of 1.7 cm in radius, 30 cm in length, centered at $(X_{cen}, Y_{cen}) = (0, 0)$ m, $\varepsilon_r = 67.0$, and $\sigma = 1.55\,\mathrm{Sm}^{-1}$. (a) 2D FDTD model and (b) Slice of the 3D FEM model at the center of the monopole antenna. White dots and dashed line show the positions of the antennas and the scattered cylinder, respectively.

Homogeneous 3D cylinders (30 cm in length) with fixed positions at $(X_{cen}, Y_{cen}) = (0, 0)$ m were simulated. One transmitter and one receiver were simulated at a time. The position of the receiver was varied from position 1 to 8 (see Fig. 7). For example, one simulation is emitting with the transmitter in position 0 (T_0) and receiving with receiver 4 (R_4, see Fig. 7(a)). A total of eight 3D simulations were conduced, and the 256 simulations required by the inverse algorithm were obtained using the symmetry of the problem. Fig. 7 shows the input of the ANN ($|E_t|/|E_{inc}|$) obtained by the 2D model and the slice of the 3D model (in the center of the active zone of the monopole, that is, the middle of the extended inner connector of the coaxial antenna). Qualitatively, a similar behaviour is observed. In an experimental situation, the measured data are the scattering coefficients (S_{ij}). Particularly, in the 3D model a lumped port was defined at the coaxial cable, and electric fields were converted to current and voltage in order to compute the S-parameters.

The reconstruction algorithm using CNN was tested with one cylinder of 1.7 cm in radius with X_{cen} and Y_{cen} located in (0.0, 0.0) cm, 30 cm in length, $\varepsilon_r = 67.0$, and $\sigma = 1.55\,\mathrm{Sm}^{-1}$. The transmission coefficients were only computed (S_{12}) and normalized to the $S_{12_{inc}}$ of the model without cylinder (coupling media only). Finally, $|S_{12}|/|S_{12_{inc}}|$ data (which ignoring the reflection coefficients is equal to the $|E_t|/|E_{inc}|$ ratio) were taken as input of the CNN, and the predicted parameters were: 1.587 cm, 0.059 cm, −0.003 cm, 67.6, and $1.58\,\mathrm{Sm}^{-1}$, for the radius, X_{cen}, Y_{cen}, relative permittivity, and conductivity, respectively. The same data were used to test the reconstruction algorithm using MLP. The predicted parameters were: 1.667 cm, 0.388 cm, −0.218 cm, 67.5, and $1.70\,\mathrm{Sm}^{-1}$, for the radius, X_{cen}, Y_{cen}, relative permittivity, and conductivity, respectively. We remark that for the 3D case both CNN and MLP inversion algorithms were tested without noise addition.

4. CONCLUSIONS

The results presented in this manuscript show that microwave tomography using amplitude-only information to reconstruct a simple geometry as an infinite cylinder is achievable with artificial neural networks. The overall quality of the reconstruction with high signal to noise ratio measurements is better with the convolutional neural network model. However, with signal to noise ratios below ∼90 dB, the position and radius estimations become similar and even worse than those of the multilayer perceptron model (although less biased). Similar behaviour is observed with the estimation of dielectric parameters of the cylinder. In both neural network models, the more robust estimations are those of the cylinder position and radius. Applications for measuring homogeneous and heterogeneous cylinders in acrylic sample holders were proposed. Good results were obtained even with heterogeneous samples with inclusions.

Finally, the three-dimensional model validates the proposed algorithms which makes this method a potential approach to develop a low-cost cylinder imaging and/or measurement setup.

ACKNOWLEDGMENT

This work was supported by a grant from the "Agencia Nacional de Promoción Científica y Tecnológica de Argentina" (Ref. PICT-2016-2303) and from the "Universidad Nacional Arturo Jauretche" (Ref. UNAJ Investiga 2017 80020170100019UJ).

REFERENCES

1. Pastorino, M., *Microwave Imaging*, John Wiley & Sons, 2010.
2. Costanzo, S., G. Di Massa, M. Pastorino, and A. Randazzo, "Hybrid microwave approach for phaseless imaging of dielectric targets," *IEEE Geoscience and Remote Sensing Letters*, Vol. 12, No. 4, 851–854, 2015.
3. Caorsi, S., A. Massa, M. Pastorino, and A. Randazzo, "Electromagnetic detection of dielectric scatterers using phaseless synthetic and real data and the memetic algorithm," *IEEE Transactions on Geoscience and Remote Sensing*, Vol. 41, No. 12, 2745–2753, 2003.
4. Li, L., W. Zhang, and F. Li, "Tomographic reconstruction using the distorted Rytov iterative method with phaseless data," *IEEE Geoscience and Remote Sensing Letters*, Vol. 5, No. 3, 479–483, 2008.
5. Li, L., H. Zheng, and F. Li, "Two-dimensional contrast source inversion method with phaseless data: TM case," *IEEE Transactions on Geoscience and Remote Sensing*, Vol. 47, No. 6, 1719–1736, 2008.
6. Bermani, E., S. Caorsi, and M. Raffetto, "Microwave detection and dielectric characterization of cylindrical objects from amplitude-only data by means of neural networks," *IEEE Transactions on Antennas and Propagation*, Vol. 50, No. 9, 1309–1314, 2002.
7. Alvarez, Y., M. Garcia-Fernandez, L. Poli, C. García-González, P. Rocca, A. Massa, and F. Las-Heras,, "Inverse scattering for monochromatic phaseless measurements," *IEEE Transactions on Instrumentation and Measurement*, Vol. 66, No. 1, 45–60, 2016.
8. Li, L., L. G. Wang, F. L. Teixeira, C. Liu, A. Nehorai, and T. J. Cui, "Deepnis: Deep neural network for nonlinear electromagnetic inverse scattering," *IEEE Transactions on Antennas and Propagation*, 2018.
9. Kamilov, U. S., D. Liu, H. Mansour, and P. T. Boufounos, "A recursive born approach to nonlinear inverse scattering," *IEEE Signal Processing Letters*, Vol. 23, No. 8, 1052–1056, 2016.
10. Goodfellow, I., Y. Bengio, and A. Courville, *Deep Learning*, MIT press, 2016.
11. Wei, Z. and X. Chen, "Deep-learning schemes for full-wave nonlinear inverse scattering problems," *IEEE Transactions on Geoscience and Remote Sensing*, 2018.
12. Jin, K. H., M. T. McCann, E. Froustey, and M. Unser, "Deep convolutional neural network for inverse problems in imaging," *IEEE Transactions on Image Processing*, Vol. 26, No. 9, 4509–4522, 2017.
13. Ronneberger, O., P. Fischer, and T. Brox, "U-net: Convolutional networks for biomedical image segmentation," *International Conference on Medical Image Computing and Computer-assisted Intervention*, 234–241, Springer, 2015.
14. Meaney, P. M., T. Zhou, D. Goodwin, A. Golnabi, E. A. Attardo, and K. D. Paulsen, "Bone dielectric property variation as a function of mineralization at microwave frequencies," *Journal of Biomedical Imaging*, Vol. 7, 2012.
15. Meaney, P. M., D. Goodwin, A. Golnabi, T. Zhou, M. Pallone, S. Geimer, G. Burke, and K. D. Paulsen, "Clinical microwave tomographic imaging of the calcaneus: A first-in-human case study of two subjects," *IEEE transactions on biomedical engineering*, Vol. 59, No. 12, 3304–3313, 2012.

16. Oskooi, A. F., D. Roundy, M. Ibanescu, P. Bermel, J. D. Joannopoulos, and S. G. Johnson, "MEEP: A flexible free-software package for electromagnetic simulations by the FDTD method," *Computer Physics Communications*, Vol. 181, 687–702, January 2010.
17. Harrington, R. F., *Time-harmonic Electromagnetic Fields*, McGraw-Hill, 1961.
18. Arslanagic, S. and O. Breinbjerg, "Electric-line-source illumination of a circular cylinder of lossless double-negative material: An investigation of near field, directivity, and radiation resistance," *IEEE Antennas and Propagation Magazine*, Vol. 48, No. 3, 38–54, 2006.
19. Attardo, E. A., A. Borsic, G. Vecchi, and P. M. Meaney, "Whole-system electromagnetic modeling for microwave tomography," *IEEE Antennas and Wireless Propagation Letters*, Vol. 11, 1618–1621, 2012.
20. Chollet, F., et al., "Keras," https://github.com/fchollet/keras, 2015.
21. Abadi, M., et al., "TensorFlow: Large-scale machine learning on heterogeneous systems," 2015, software available from tensorflow.org. [Online]. Available: https://www.tensorflow.org/.
22. Ruder, S., "An overview of gradient descent optimization algorithms," arXiv preprint arXiv:1609.04747, 2016.
23. Nair, V. and G. R. Hinton, "Rectified linear units improve restricted boltzmann machines," *Proceedings of the 27th International Conference on Machine Learning (ICML-10)*, 807–814, 2010.
24. Kingma, D. P. and J. Ba, "Adam: A method for stochastic optimization," arXiv preprint arXiv:1412.6980, 2014.
25. Sihvola, A., "Electromagnetic mixing formulas and applications," *IET Electromagnetic Waves Series*, Vol. 47, 1999.